Improved control of floating offshore wind turbine motion by using phase-resolved wave reconstruction and forecast

Shawn T. Albertson[1], *Mojgan Gharankhanlou*[1], *Stephanie C. Steele*[1], *Stephan T. Grilli*[1], *Jason M. Dahl*[1], *Annette R. Grilli*[1], *M. Reza Hashemi*[1], *Yuksel R. Alkarem*[2,3], *Kimberly Huguenard*[4]

(1) Department of Ocean Engineering, University of Rhode Island Narragansett, RI, USA
(2) Department of Civil and Environmental Engineering, University of Maine Orono, ME, USA
(3) Advanced Structures & Composites Center, Orono, ME, USA
(4) Department of Mechanical Engineering, University of Maine, Orono, ME USA

ABSTRACT

Floating Offshore Wind Turbines (FOWT) can be actively controlled to minimize their wave induced motions, improving wind energy harvesting efficiency and increasing structural life by reducing fatigue loads. Here, we report on the development and validation of Wave Reconstruction and Prediction (WRP) algorithms that improve the active control of floating structure motions, achieved, e.g., by moving mass or ballast. Specifically, given a sensing method, here assumed to be LiDAR-like, that acquires dense spatiotemporal surface elevation data at some distance from the FOWT in the incident wave direction, we present and validate deterministic WRP algorithms, based on fast nonlinear and dispersive Lagrangian wave models, and integrate their predictions with in-the-loop hardware and a real time control system that is informed by computations with a digital twin (DT) model of the floating structure. We implement multiple WRP wave models including a model based on linear wave theory (LWT) with a correct dispersion accounting for nonlinearity (LWT-CDR) and a 2nd-order "Choppy" wave model with improved nonlinear dispersive properties (ICWM), initialized with a linear prediction. Although we run laboratory experiments of the complete system, which are reported elsewhere, here the WRP implementation is validated against fully nonlinear potential flow simulations in a Numerical Wave Tank (NWT), which shows both LWT-CDR and ICWM models appear to provide reasonable short-term predictions at the float. Implications for the real time control system are discussed; in a companion paper, the use of short-term wave predictions with the WRP is shown to improve the real time control of float motions in waves.

KEYWORDS: Phase-resolved wave prediction, motion control systems, floating offshore wind turbines

INTRODUCTION

Many offshore wind farms are in development along the US East Coast, with about 3GW of total installed power, that will be equipped with turbines installed on static foundation support structures. The current goal of the US administration, however, is to install ten times as much offshore wind power in US waters by 2030, and to meet this goal, it will be necessary to develop farms also in deeper waters, beyond the continental shelf, made of floating offshore wind turbines (FOWT). In some areas of the US, such as the Gulf of Maine or the West Coast, which feature a narrow shelf, FOWTs are the only viable option.

FOWTs are composed of a float, usually a single spar or multiple connected cylinders, anchored using a slack mooring system, and a support structure attached to the float (e.g., a cylindrical tower with varying inertia), with on top a nacelle that includes an electric motor and a transmission system, on which the turbine blades are attached. Such a floating and top heavy system may significantly oscillate under the action of wind, but mostly ocean waves, particularly in heavy sea states, with the roll/pitch motions causing an eccentricity of the heavy nacelle that significantly increases structural stresses, e.g., at the tower bottom, hence reducing the FOWT fatigue life, and significant motions of the turbine blades that will affect their aerodynamic efficiency and, hence, their energy harvesting ability.

To improve the energy capture and increase the fatigue life of such systems (which both affect the levelized cost of electricity; LCOE), it is thus important to minimize the FOWT wave-induced motions, which can be achieved through using active control methods, e.g., through moving mass or water ballast within the FOWT float. Such methods are actuated by Model Predictive Control (MPC) algorithms that can anticipate the float motions, usually based on a model or "digital twin" (DT) of the system that assimilates the past motion history (e.g., Casanovas, 2014; Ma et al., 2018). Such algorithms are reviewed in our companion paper (Steele et al., 2023). Earlier studies, however, have shown that the optimal control of a FOWT (or any float) motions requires predicting the wave excitation force a short time in the future (e.g., 5-10 s; Ma et al., 2018), as a result of the causality principle in irregular waves (e.g., Babarit and Clément, 2006; Fusco and Ringwood, 2010). It should be stressed that, similar to the optimal control of wave energy converters (WECs; e.g., Wu et al., 2009; Grilli et al., 2011b; Faedo et al., 2017; Hals et al., 2011; Zou et al., 2017), it is key in this problem to accurately predict the phase of waves impacting the FOWT float, since any significant phase mismatch will impede the control and, in the worst-case scenario, make matters worse. Indeed, while in WECs, the control aims at maximizing the wave-induced motions of some mechanical system, for FOWTs, control aims at minimizing float motions; hence, a faulty

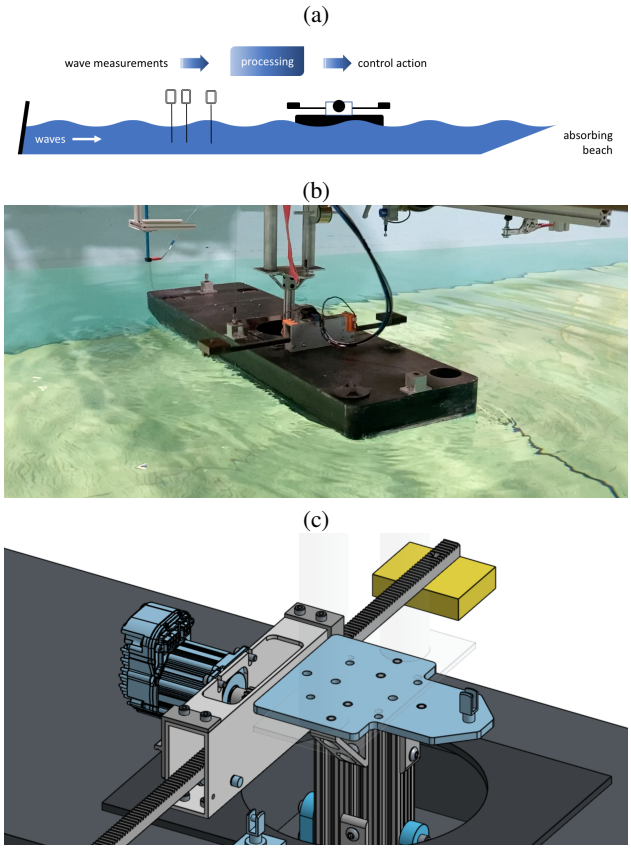

Fig. 1: (a) Sketch of FOWT proxy barge model in wave tank, to test real time application of WRP models that forecast waves at the float, based on surface elevations measured at upstream gauges, which are used in DT-MPC control algorithm that actuates moving masses (see (c)). (a,b) Barge in tank under staff allowing heave/roll motions in wavemaker generated waves. (c) Details of mass slider active control system and heave/roll post to attach model to tank carriage heave staff (see (b)).

control due to a phase-mismatch, could, instead, increase these motions. In Steele et al. (2023), we demonstrate that FOWT motion control with a DT-MPC can indeed be significantly improved by using a short-term forecast $\mathscr{O}(T_p)$ (with T_p the sea state's peak spectral period) of the phase-resolved waves (and their loads) that will impact the float, obtained from a wave reconstruction and prediction (WRP) algorithm.

In this paper, we report on the development and validation of such WRPs. Building on earlier work by our team (e.g., Grilli et al., 2011a; Nouguier et al., 2014; Desmars et al., 2020), we assume that a remote sensing system is available (e.g., based on a LiDAR camera, LC, or similar) that can provide a dense spatiotemporal data set of surface elevations measured at some distance from the float in the direction of incident waves. On this basis, we develop, compare, and apply physics-based linear/weakly nonlinear deterministic WRP models, fast enough to predict future phase-resolved waves at the float in real time. WRP results are validated against those of a fully nonlinear numerical wave tank (NWT).

Deterministic wave forecasting approaches use spatiotemporal wave measurements near a location of interest (e.g., a FOWT float) to initialize models that predict how waves propagate to a new location (e.g., Wu, 2004; Fusco and Ringwood, 2010; Blondel-Couprie et al., 2013; Nouguier et al., 2014; Desmars et al., 2020). For short time scales and moderate sea states, linear models may be sufficiently accurate, but for higher sea states wave nonlinearity becomes important and causes amplitude dispersion effects that introduce phase shifts that affect the timing of wave loading on the float. Hence, models featuring the required physics to represent such effects should be used. This is further detailed hereafter.

Wu (2004) laid out the basic groundwork in this area and applied WRP models, to both simulated and measured wave data, based on linear (LWT) or 2nd-order wave theory, and on the higher-order spectral method (HOS) (Dommermuth and Yue, 1987), which allows simulating the propagation of highly nonlinear waves. Compared to other methods discussed here, HOS (see also, Ducrozet et al., 2016) has a much higher computational cost but represents nonlinear sea states very well. Wu (2004) also established a foundation for estimating the space-time region where an accurate forecast can be made for a given set of spatiotemporal wave data; this "prediction zone" was estimated based on the speed of energy transport in the wave field, i.e., the (linear) group velocities of the lowest and highest frequency waves in the sea state. This approach has since been applied in many studies including Blondel-Couprie et al. (2013), Naaijen et al. (2014); Desmars et al. (2020), and the present one.

Models based on LWT are the most widely used and have been shown to be effective in many applications. For example, both Dannenberg et al. (2010) and Naaijen et al. (2012) showed how such models can be used to predict future sea states to advise offshore operations such as heavy lifting. Although sharing the same objective as our work, to provide wave forecasting in real time, such studies may not need to predict wave phases as accurately as required here, as discussed before. Regarding nonlinear WRP methods, the challenge is to use a model that will feature sufficient physics to accurately simulate both wave shape and phase, while being efficient enough to be run in real time, together with the float DT-MPC control algorithm. In this respect, earlier work has illustrated the advantages of using nonlinear Lagrangian (i.e., Gerstner-type) rather than Eulerian (i.e., Stokes-type) wave models, since the former models feature nonlinear wave properties that are one-order of nonlinearity higher than the equivalent-order Eulerian model (e.g., Guérin et al., 2019). Thus, in their WRP model based on LiDAR-like data, Grilli et al. (2011a) implemented the Lagrangian wave model "Choppy I" (CWM) (Nouguier et al., 2009), which represented second-order effects in a highly efficient manner, improving the shape but not the dispersive properties of waves, which are the same at 1st- as 2nd-order. Nevertheless, CWM was shown by Nouguier et al. (2014) to be effective when applied to synthetically generated two-dimensional (2D) LIDAR-like data, meant to replicate actual wave measurements by a LC at grazing incidence. To represent wave dispersive properties to 3rd-order, which includes amplitude dispersion effects, the 2nd-order Lagrangian Choppy II model (CWM2) was developed by Nouguier et al. (2015), and later applied to the WRP problem by Desmars et al. (2020), who found it to be accurate but too computationally demanding to be applied in real time. As a compromise, Guérin et al. (2019) developed the so-called "Improved choppy wave model" (ICWM), that improved the dispersive properties of CWM without significantly increasing its numerical complexity. Desmars et al. (2020) showed that using ICWM greatly improved the wave forecast accuracy when nonlinearity is significant, without the computational cost of CWM2. This hopefully would allow to run the model in real time, which they did not demonstrate in their work. Additionally, these authors tested a LWT model with improved dispersion (LWT-CDR), whose computational cost is even lower. Using a HOS solution as a reference as well as wave tank data, Desmars et al. (2020) clearly showed the large improvement in wave prediction (particularly phase) accuracy resulting from using a modified dispersion relationship (e.g., ICWM or LWT-CDR), as compared to results of WRP models based on LWT and CWM.

Based on these findings, in this work, we have developed WRP algorithms based on the various Lagrangian or LWT models discussed above and implemented them to be used for real time in-the-loop wave forecast, in combination with a float control algorithm (see, Steele et al., 2023). In the following, we provide results of applying these WRP models on both

experimental data as well as data from a fully nonlinear NWT. To test our algorithms in real time, we built a proxy FOWT float and control system in the form of a scale model of a barge with two horizontally moving masses actuated by an electric motor and a slider system (Fig. 1) that we tested in the University of Rhode Island's (URI) wave tank, together with the acquisition of LiDar like data using a set of wave gauges and predictions of wave loads on the float using the WRPs.

SYSTEM OVERVIEW

Given a float equipped with an active control system (e.g., the slider mass system of Fig. 1), assuming spatiotemporal wave measurements are made upstream of the float, here using wave gauges, the WRP deterministically reconstructs and propagates incident waves up to the location of the float, allowing to estimate future wave loads that are assimilated into the DT model, together with the history of past float motions, to simulate the future float motions and inform the MPC control algorithm that actuates the control system (see, Steele et al., 2023). Assuming a fairly stationary wave field (i.e., one with a slowly changing energy density spectrum) and given an acquisition time window $[t_a = t_0 - \Delta t_a, t_0]$ at current time t_0, where Δt_a is the acquisition time, the WRP provides a continuous short-term wave forecast, at $t_p = t_0 + \Delta t_p$, at the float location, where Δt_p is the prediction time, fast enough to allow for real time DT-MPC computations that actuate the control system to adapt to changing float motions in irregular waves. The reconstruction allows estimating the WRP model parameters that are then used to propagate waves to the float location x_e at time t_p. This process is continuous as time progresses.

Besides the accuracy of the wave prediction, computational efficiency is a key consideration for developing a useful WRP-DT system, since the prediction must be issued faster than real time to allow the DT-MPC to also perform computations. In the idealized experimental set-up used to demonstrate and validate our system (Fig. 1), wave measurements are made at spatially fixed wave gauges, but the WRP models considered here can assimilate arbitrary sets of LiDAR-like unstructured spatiotemporal data. Additionally, here the WRPs are validated based on uni-directional laboratory waves and hence their equations are simplified to one spatial dimension (1D). However, the proposed models can readily be extended to 2D (e.g., Nouguier et al., 2014; Kim et al., 2023), although the computational effort will be greater.

Fig. 2 shows a flow chart of the WRP-DT-MPC system, used in the 1D experimental set-up of Fig. 1, and its hardware, which besides wave gauges includes a data acquisition device (DAQ) and a PC computer. The DAQ continuously acquires analog data from upstream wave gauge, which it transfers to the PC, whenever a new dataset of length Δt_a is available. The WRP running on the PC processes these datasets and issues a wave prediction at the float location, which is then used by the DT-MPC algorithm, together with past float motions, to compute the control command and actuate the active control system to modify float motions resulting from future incident waves. The DAQ simultaneously generates and applies the corresponding signal to the control system motor controller, here actuating the mass-slider. Efficient and robust computations as well as synchronization are thus of the utmost importance to develop a fully functional system.

For the purpose of development and validation, the WRP-DT model was implemented two ways, so that the wave predictions at the float could be based on wave data: (i) either pre-calculated and saved, or (ii) generated in real time and loaded in the loop. In both cases, parameters defining the problem set-up and WRP model characteristics need to be provided, such as Δt_a, Δt_p, the cut-in (low)/cut-off (high) frequencies $[\omega_l, \omega_h]$ of wave components having significant energy in the sea state, and number N of wave harmonics of frequency ω_n and amplitude A_n used to reconstruct and predict waves (this is discussed later). In this work we also assume that the water depth h_0 is such that we have deep

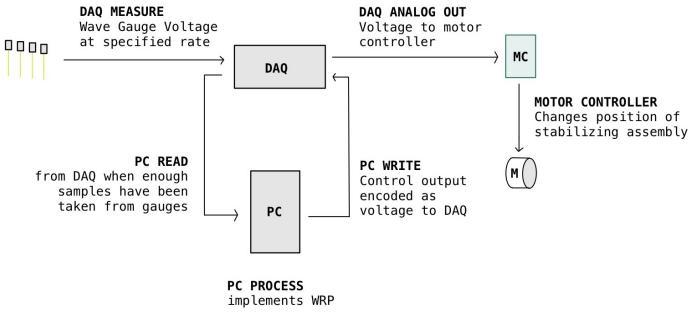

Fig. 2: Flow chart of the WRP-DT-MPC system and its hardware used in experimental set-up of Fig.1. Wave gauge data is recorded by the DAQ and processed on the PC, on which the WRP-DT is implemented; using predicted waves and past float motions, a control action is given by the MPC to the DAQ, which actuates the slider-mass control system motor.

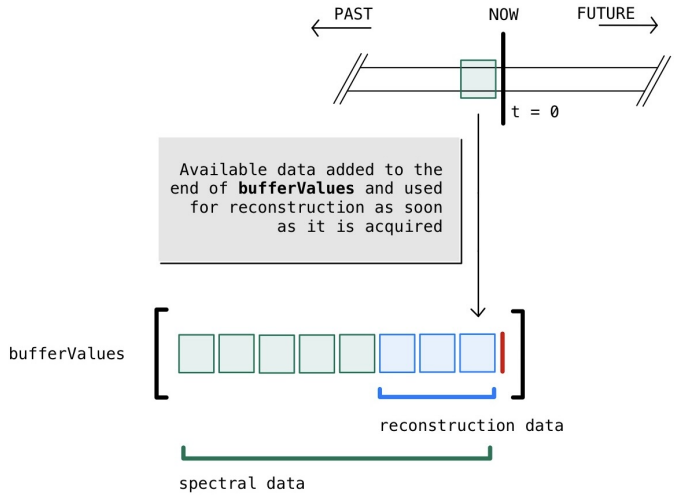

Fig. 3: Flowchart showing how small wave datasets of duration Δt_d are continuously acquired at gauges and added to a buffer; once Δt_a worth of data is acquired, this data is processed by the WRP and transmitted to the DT-MPC model by the DAQ (see Fig. 2).

water waves, which implies $k_n h_0 \geq \pi, \ \forall\, n$; hence, based on the linear wave dispersion relationship (Dean and Dalrymple, 1990), we have,

$$k_{0n} = \frac{\omega_n^2}{g}; \quad c_{n0} = \frac{\omega_n}{k_{0n}} = \frac{g}{\omega_n}; \quad c_{g0n} = \frac{1}{2} c_{n0} = \frac{g}{2\omega_n}, \tag{1}$$

for the wavenumber, phase speed, and group velocity, respectively, where g is the gravitational acceleration and the subscript 0 refers to deep water parameters. Whether simulated or deployed in the wave tank one also needs to specify the number M and locations x_m of wave gauges measuring incident waves. As we shall see, the prediction zone, i.e., the space-time domain where wave predictions exist, is function of the slowest and fastest group velocities of energetic waves in the sea state, i.e., using Eq. 1, $c_{g0h} = g/(2\omega_h)$ and $c_{g0l} = g/(2\omega_l)$, respectively.

Fig. 3 shows how the system, by way of the DAQ controlled by the PC (Fig. 2), continuously loads small wave data sets of length Δt_d into a buffer, as they become available, and combines those with previously collected data to create a reconstruction data set of length Δt_a. Hence, at any given time, represented here by $t_0 = 0$, only part of the buffer is used as WRP data and the potential update rate of wave predictions is thus $\Delta t_d \ll \Delta t_a$. On startup, the buffer needs to fill-up to acquire at least Δt_a worth of wave data, before an initial wave prediction can be accurately issued.

DETERMINISTIC WAVE RECONSTRUCTION/PREDICTION

A deterministic physics-based WRP assumes that the sea state is represented by the superposition of many constituent waves, including potential nonlinearities resulting from wave-wave interactions. Using a model based on LWT, reconstruction is equivalent to a simple Fourier superposition, with the phase and group velocity of each constituent wave based on the linear dispersion relationship, as detailed before (Eq. 1). In the CWM, the phase speed of each constituent is still based on the same equation, but wave geometry is modified in a manner similar to 2nd-order Stokes wave theory, with a trough to crest asymmetry. For a 1D problem, the CWM performs a Hilbert transform that corrects abscissa x and is in fact identical to Gerstner's trochoïdal wave theory; for 2D problems, the CWM requires performing a Riez Transform (Nouguier et al., 2009, 2014). In the ICWM, corrections for Stokes drift and a mean water level (MWL) increase $\overline{\eta}$ are included, which also result in an amplitude dispersion correction for the phase speed (Guérin et al., 2019).

For a single wave component of amplitude A and frequency ω propagating in deep water, Stokes drift causes a depth-averaged current, $\mathscr{U}_{s0} = k_0 A^2 \omega = \varepsilon^2 c_0$, with $\varepsilon = k_0 A$, the wave steepness. When considering this current in the ICWM, a Doppler shift of the wave frequency occurs, with, $\tilde{\omega} = \omega + k_0 \mathscr{U}_{s0}/2$, and phase speed becomes, $c_{NL} = c_0(1+\varepsilon^2/2)$, which matches the 3rd-order Eulerian (Stokes) solution (Guérin et al., 2019). Finally, assuming that the vertical datum $z = 0$ is at the MWL, wave elevations in the ICWM are corrected by, $\overline{\eta} = kA^2/2$. For an irregular sea state with N components, represented by a spectrum $S(\omega_n) = A_n^2/(2\Delta\omega)$ $(n = 1, ...N)$, these formula become,

$$\mathscr{U}_{s0} = \sum_{n=1}^{N} k_{0n} A_n^2 \omega_n \quad ; \quad \overline{\eta} = \frac{1}{2} \sum_{n=1}^{N} k_{0n} A_n^2 \quad ; \quad \tilde{\omega}_n = \omega_n + k_{0n} \mathscr{U}_{s0}/2. \tag{2}$$

In the WRP model, at time t_0, parameters of a given wave model (LWT, ICWM, etc.) are first computed by minimizing the mean square difference (LSM) between reconstructed and observed wave elevations $\tilde{\eta}_{jk}(x_j, t_k)$, at J locations x_j and K times t_k over the acquisition time interval $[t_a, t_0]$, with a temporal resolution Δt (or $f_a = 1/\Delta t$ the data acquisition frequency). To simplify notations, measured surface elevations are defined as $\tilde{\eta}_\ell$ with $(\ell = 1, ..., L = J \times K)$. Model parameters, which are functions of wave component amplitudes and phases, then allow in the prediction phase of the WRP to accurately compute (i.e., propagate the reconstructed) waves at the float location x_e, and time of interest t_p, provided these are selected within the proper space-time prediction zone. In the following real time framework, the time at which wave data is reconstructed with the WRP is set to $t_0 = 0$, meaning that positive times are in the future, e.g., for estimating the control command at $t_p = \Delta t_p$, while negative times refer to the WRP data acquisition over $[t_a = -\Delta t_a, 0]$.

Note that, to accurately estimate the range of energetic frequencies in the sea state, the spectrum $S(\omega_n)$ is first calculated based on wave measurements acquired for a larger number of dominant/peak wave period T_p (here a minimum of 30) than will be typically used for a standard reconstruction acquisition time window (i.e., $\Delta t_a = 6 - 12T_p$). Low and high frequency cut-offs $[\omega_l, \omega_h]$ are then found based on a minimum energy in the spectrum S_{min} (set here to 5% of the maximum S_{max}); these frequency cut-offs will be used to compute the allowable prediction zone. As more wave data is being gradually acquired as part of the WRP, the spectrum and corresponding $[\omega_l, \omega_h]$ values are iteratively adjusted, which accounts for slow changes in the sea state. Note, the spectrum also allows computing the sea state's significant wave height, $H_s = 4\sqrt{m_o}$, where m_o is the zero-th moment of the spectrum, and dominant/peak wavelength, $L_{0p} = gT_p^2/(2\pi)$, where T_p corresponds to the period associated with the highest energy content in the spectrum. Details of the various wave models used in the WRP model are provided next.

Linear wave models (LWT, LWT-CDR)

In LWT, a 1D surface elevation is represented as the linear superposition,

$$\eta_L(x,t) = \sum_{n=1}^{N} \{a_n \cos\Psi_n + b_n \sin\Psi_n\} \text{ with, } \Psi_n = (k_{0n}x - \omega_n t), \tag{3}$$

with k_{0n} given by Eq. 1 as a function of ω_n, uniformly distributed within $[\omega_l, \omega_h]$. Eq. 3 is similar to the standard Fourier representation of observed data used to compute the sea state's energy density spectrum $S(\omega_n) = (a_n^2 + b_n^2)/(2\Delta\omega)$, with a frequency resolution $\Delta\omega$.

In LWT-CDR, a correction for amplitude dispersion is made by substituting $\omega_n = \tilde{\omega}_n$ from Eq. 2 in Eq. 3. In this case, the LSM computation of the model parameters (a_n, b_n) based on measured data $\tilde{\eta}_\ell$, requires iterations because of the dependence of $\tilde{\omega}_n$ on these parameters.

Choppy and improved Choppy wave models (CWM, ICWM)

For 1D problems, the CWM or ICWM nonlinear free surfaces are obtained by shifting the abscissa x where the linear elevation is computed to $x + D(x,t)$, based on the space and time dependent Hilbert transform,

$$D(x,t) = \sum_{n=1}^{N} \{-a_n \sin\Phi_n + b_n \cos\Phi_n\} \text{ with, } \Phi_n = (k_{0n}x - \tilde{\omega}_n t). \tag{4}$$

Assuming that the horizontal (Lagrangian) displacement represented by $D(x,t)$ is small, the nonlinear free surface is explicitly found as,

$$\eta_{NL}(x,t) = \sum_{n=1}^{N} \{a_n \sin\Phi_n^{'} + b_n \cos\Phi_n^{'}\} + \mu\overline{\eta}, \tag{5}$$

with the phases,

$$\Phi_n^{'} = k_{0n}(x - D(x,t)) - \tilde{\omega}_n t = \Psi_n - k_{0n}\{D(x,t) + \frac{1}{2}\mu\mathscr{U}_{s0}\, t\}, \tag{6}$$

where for ICWM, $\mu = 1$, and $\mathscr{U}_{s0}$, $\overline{\eta}$ and $\tilde{\omega}_n$ are computed with Eq. 2, and all of these parameters are zero for CWM.

Note that, the (ω_n, k_{0n}) values used in CWM and ICWM are the same as used in the LWT model, whose coefficients are used to initialize the nonlinear models. In both of these, the LSM solution also requires iterations, both because of $D(x,t)$ and $\overline{\eta}$ and, for ICWM since $\mathscr{U}_{s0}$ and $\tilde{\omega}_n$, are also functions of the model coefficients.

Computation of model coefficients

In the reconstruction phase of the WRP, given a data set of measured surface elevations $\tilde{\eta}_\ell$ with $(\ell = 1, ..., L)$ and for $N \ll L$, the model coefficients (a_n, b_n) are computed with Eq. 3 for LWT and Eqs. 4-6 for CWM/ICWM, by minimizing the error (or LSM cost) function,

$$C = \frac{1}{L} \sum_{\ell=1}^{L} (\eta_{L/NL}(x_\ell, t_\ell) - \tilde{\eta}_\ell)^2, \tag{7}$$

in the least square sense, yielding for $q = 1, ..., N$,

$$\frac{\partial C}{\partial a_q} = 0, \quad \frac{\partial C}{\partial b_q} = 0 \iff \mathsf{A}_{mn}^i p_n = \mathsf{B}_m^i; \text{ for } m, n = 1, ..., 2N, \tag{8}$$

which is iteratively solved for $p_n^{i+1} = a_n^{i+1}, p_{N+n}^{i+1} = b_n^{i+1}$ (i representing the current iteration), with,

$$\begin{aligned}
\mathsf{A}_{mn}^i &= \sum_{\ell=1}^{L} k_n^{-3/2} \left(\cos\Phi_{n\ell}^{i'} + \frac{\mu}{2} a_n^i k_n^{-1/2}\right) P_{m\ell}(a_m^i, b_m^i), \\
\mathsf{A}_{m,N+n}^i &= \sum_{\ell=1}^{L} k_n^{-3/2} \left(\sin\Phi_{n\ell}^{i'} + \frac{\mu}{2} b_n^i k_n^{-1/2}\right) P_{m\ell}(a_m^i, b_m^i), \\
\mathsf{A}_{N+m,n}^i &= \sum_{\ell=1}^{L} k_n^{-3/2} \left(\cos\Phi_{n\ell}^{i'} + \frac{\mu}{2} a_n^i k_n^{-1/2}\right) Q_{m\ell}(a_m^i, b_m^i), \\
\mathsf{A}_{N+m,N+n}^i &= \sum_{\ell=1}^{L} k_n^{-3/2} \left(\sin\Phi_{n\ell}^{i'} + \frac{\mu}{2} b_n^i k_n^{-1/2}\right) Q_{m\ell}(a_m I, b_m I),
\end{aligned} \tag{9}$$

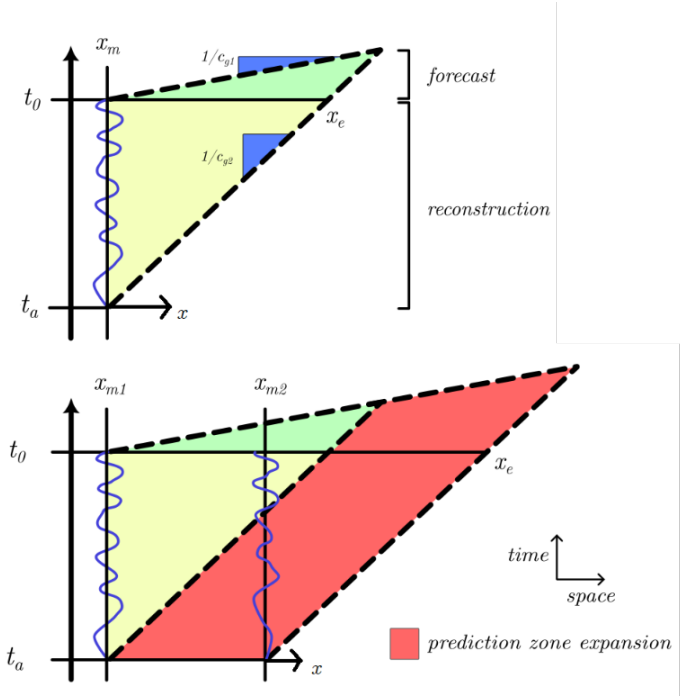

Fig. 4: Linear wave prediction zone at location x_e, for both a single measurement location at x_m (top) and multiple measurement locations within $[x_{m1}, x_{m2}]$ (bottom), based on the fastest/slowest group velocities, c_{g1} and c_{g2}, respectively, in the sea state. The prediction zones narrows in time as $x - x_{mi}$ increases, until it eventually disappears. For a range of spatial measurement locations the prediction zone area is increased.

and,

$$\mathsf{B}_m^i = \sum_{\ell=1}^{L} \tilde{\eta}_\ell \, P_{m\ell}(a_m^i, b_m^i), \quad \mathsf{B}_{N+m}^i = \sum_{\ell=1}^{L} \tilde{\eta}_\ell \, Q_{m\ell}(a_m^i, b_m^i), \tag{10}$$

where, given (a_m, b_m) values we have,

$$\begin{cases} P_{m\ell} = \cos\Phi_{m\ell}^{'} - \lambda k_m^{-1/2} \left(a_m \sin\Phi_{m\ell}^{'} - b_m \cos\Phi_{m\ell}^{'} \right) \Big(\sin\Phi_{m\ell} \\ -\mu a_m \omega_m k_m^{-1/2} t_\ell \left[k_m^{-1/2} \left(a_m \cos\Phi_{m\ell} + b_m \sin\Phi_{m\ell} \right) + 1 \right] \Big) + \mu a_m k_m^{-1/2}, \\ Q_{m\ell} = \sin\Phi_{m\ell}^{'} - \lambda k_m^{-1/2} \left(a_m \sin\Phi_{m\ell}^{'} - b_m \cos\Phi_{m\ell}^{'} \right) \Big(-\cos\tilde{\Phi}_{m\ell} \\ -\mu b_m \omega_m k_m^{-1/2} t_\ell \left[k_m^{-1/2} \left(a_m \cos\Phi_{m\ell} + b_m \sin\Phi_{m\ell} \right) + 1 \right] \Big) + \mu b_m k_m^{-1/2}. \end{cases} \tag{11}$$

Eq. 11 corresponds to ICWM when $\lambda = \mu = 1$; for CWM, $\lambda = 1$ and $\mu = 0$, and for LWT, both of these are zero. For CWM and ICWM, the iterative solution is initialized with the LWT solution for $i = 1$.

Prediction Zone

For a given spatiotemporal data set of surface elevations, acquired over time Δt_a prior to current time t_0, an accurate prediction is expected at the float location x_e at time $t_0 + t_p$, provided these are within the allowable prediction zone. To establish this prediction zone, following Wu (2004), we note that waves can only be predicted based on the reconstructed wave field, if the corresponding energetic wave components have had sufficient time to propagate to location x_e; otherwise, no meaningful "information" has is available and predicted waves will have a very large error. Since the speed of wave energy propagation, i.e., the group velocity c_{g0}, is frequency dependent (see Eq. 1), the prediction zone can be identified by tracking the propagation of the energy of the two lowest and highest frequency energetic wave components $[\omega_l, \omega_h]$ in the sea state, defined before, i.e., at speed $c_{g1} = c_{g0l}$ and $c_{g2} = c_{g0h}$, respectively, with $c_{g1} > c_{g2}$. Hence, for a given location x_e, there exists a time interval $[t_{min}, t_{max}]$ corresponding to the temporal prediction zone boundaries at the said location.

For measurements made at a single location/gauge x_m, Fig. 4 (top) shows a graphical representation of these properties in the (x,t) plane, which outlines the expected prediction zone, assuming LWT (i.e., no amplitude dispersion effects). If wave gauges span a spatial range $[x_{m1}, x_{m2}]$, Fig. 4 (bottom) shows that the prediction zone is extended since the measurements now span a region of both time and space.

Reconstruction bandwidth

The WRP algorithm requires selecting N wave component with relevant frequencies to be used in the LSM problem that performs the reconstruction, i.e., Eqs. 7 and 8, with LWT Eq. 3 or CWM/ICWM Eqs. 4-6. Hence, to ensure an accurate reconstruction, one also needs to select the highest and lowest frequencies ω_n, or wavenumbers k_{0n}, based on the shortest and longest spatial scales (or resolution) one aims to achieve at time t_p, for waves in the prediction zone.

Accordingly, the smallest resolved wavenumber in the WRP is defined as, $k_{0,\min} = 2\pi/L_{\max}$, with $L_{\max}$ denoting the largest predictable region at reconstruction time t_0. For instance, in Fig. 4, $L_{\max} = x_e - x_{m1}$, with $x_e = x_{m2} + c_{g2} t_a$ and (x_{m1}, x_{m2}) the farthest and nearest locations where wave measurements are made with respect to the experiment's or prediction location x_e, respectively. Likewise, the largest resolved wavenumber $k_{0,\max}$ can be determined as a function of either the spatial Δx or temporal Δt resolution. If measurements are made at a very high spatial resolution, such as could be achieved with a LC, the smallest distance between two data points, $L_{\min}$, could be used to determine the maximum wavenumber $k_{0,\max} = 2\pi/L_{\min}$. However, in our specific experimental setup, wave measurements are only made at coarse spatial intervals, but at a high frequency f_a, so the largest wavenumber is defined as that corresponding to the Nyquist frequency $f_N = 1/(2\Delta t)$, i.e., $k_{\max} = (\pi/\Delta t)^2$. For high frequency sampling, however, this yields unnecessarily large wavenumbers, e.g., $k_{0,\max} = 987$ m^{-1} for 10 Hz, so in practice, the upper bound for the frequency in the WRP is selected, similar to the group velocities, using the high frequency cutoff for energetic waves in the spectrum, hence, as $k_{0,\max} = \omega_h^2/g$.

Once the $[k_{0,\min}, k_{0,\max}]$ or $[\omega_{\min}, \omega_{\max}]$ values are selected in the WRP, a set of N frequencies ω_n are linearly distributed between these cut-offs, with corresponding k_{0n} computed with Eq. 1, which are used with the various model equations and the wave measurements to compute the (a_n, b_n) coefficients in the wave reconstruction; $N = 100$ frequencies were used for all results discussed here.

Prediction error metrics

Applications of the WRP algorithm are presented in the next section. In each case, we assume an acquisition time duration Δt_a prior to current reconstruction time t_0, and use a single prediction location x_e (that of the float) and time series t_s which spans the expected temporal prediction zone given our spatial measurement configuration and spectral content. For each model used in the WRP, wave predictions $\eta(x_e, t_s)$ are compared with actual wave elevations (simulated or observed) for times selected within the prediction zone whose limits can be seen as in Fig. 4.

The accuracy of the surface elevation prediction is assessed with the error metric,

$$\mathscr{E}(x_e, t_s) = \frac{1}{R H_s} \sum_{r=1}^{R} \mid \eta(x_e, t_s) - \tilde{\eta}(x_e, t_s) \mid_r \tag{12}$$

	x_1	x_2	x_3	x_4	x_5	x_6	x_7	x_e
x/L_p	-1.92	-1.28	-0.9	-0.58	-0.32	-0.13	0	2

Table 1: Relative location of measurement wave gauges $g_i, i = 1,...7$ and g_e at the float, with respect to the peak spectral wavelength L_p, used in the wave tank/NWT.

which is the absolute difference between predictions and observations at x_e, for time values t_s selected within the prediction zone, scaled by the significant wave height, and ensemble averaged over R realizations of the WRP. These realizations correspond to a series of predictions made based on independent, but overlapping, spatiotemporal data sets of wave elevations acquired in the same sea state for identical acquisition time duration Δt_a.

Of particular interest is to assess this error over a useful time series, namely the time in the future up to the prediction zone time boundary, or $[0, t_{max}]$. This can be obtained by averaging $\mathscr{E}(x_e, t_s)$ over this time interval, as,

$$\mathscr{E}^F = \frac{1}{t_{max}} \int_0^{t_{max}} \mathscr{E}(x_e, t) dt, \tag{13}$$

which provides a global error metric quantifying the surface elevation misfit over a relevant temporal domain.

As indicated before, however, even more important than errors on surface elevations, we are concerned in this problem with potentially large errors in wave phases that could cause faulty control commands to be issued in the float control system. To do so, we compute a cross-correlation function, which convolves surface elevations computed in the WRP to those serving as reference (i.e., observed or computed with a NWT), with a varying time lag τ. The time lag τ_{max} that maximizes this correlation is then computed and used as an overall error metric for the phase mismatch resulting from the WRP. Again, using the future time interval $[0, t_{max}]$ for $x = x_e$, we thus compute,

$$C(\tau) = \frac{1}{t_{max}} \int_0^{t^{max}} \tilde{\eta}(x_e, t)\, \eta_{L/NL}(x_e, t+\tau)\, \mathrm{d}t \tag{14}$$

which yields τ_{max} such that $C(\tau_{max})$ is maximum, and the error metric on wave phases is defined as, $\mathscr{E}^P = \mid \tau_{max} \mid / T_p$. In results, this misfit metric is ensemble-averaged over R realizations.

NUMERICAL/PHYSICAL EXPERIMENT

While many laboratory experiments were performed in this project, to which the WRP models were applied, as these include additional sources of uncertainty and noise (e.g., wavemaker generation, instrumentation,...), we first assessed the efficiency and accuracy of the models for real time wave predictions, in comparison to "numerical experiments" set-up and run in a similar geometry as the experiments (Fig 5), with a Numerical Wave Tank (NWT) based on fully nonlinear potential flow theory (FNPF) (e.g., Grilli and Subramanya, 1996; Grilli and Horrillo, 1997; Grilli et al., 2020). FNPF theory does not include any assumptions besides irrotational flow, and has been shown to be very accurate to simulate wave generation and propagation in many earlier applications (see references). The same experiments were then repeated in the wave tank, in combination with the DT-MPC models applied to the barge FOWT proxy of Fig. 1 (see, Steele et al., 2023).

For the various models considered here, in each case, the WRP algorithm is applied to predict waves at the float locations x_e, using actual or simulated time series of waves acquired over time Δt_a at 7 numerical wave gauges ($g_i, i = 1,...7$; Table 1). To assess the accuracy of the prediction, another gauge is deployed at x_e (g_e) next to the float (Fig. 5).

Five numerical/physical experiments were considered here, referred to as (**A** - **E**), with parameters listed in Table 2. In each case, irregular

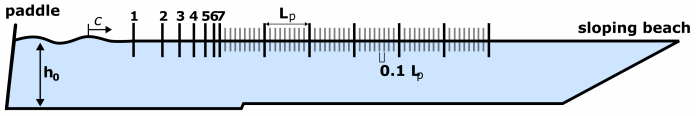

Fig. 5: Physical/NWT wave tank geometry. Gauges 1-7 measure waves over Δt_a in the WRP, while other gauges g_e (thick black lines) are at distances nL_p ($n = 1,...$) from gauge 7 and mark the float location x_e.

waves were generated in the tank/NWT using a flap wavemaker, with a target significant wave height H_s different for each case but a peak period $T_p = 1.0$ s identical for each case. With a water depth in the tank, $h_0 = 1.4$ m, $L_p = L_{0p} = 1.56$ m, the deep water wavelength, which yields increasing levels of nonlinearity in waves from cases **A** to **E**, as quantified by the peak wave steepness H_s/L_p listed in the table. As indicated, in the following, results are only presented for the NWT experiments, while results of physical experiments can be found in our companion paper (Steele et al., 2023). In the NWT the bottom geometry is identical to the physical tank(Fig. 5), with a sloping beach in the far end where energy dissipation by breaking is simulated using an absorbing beach. Although other wave generations methods are available in the NWT, as in the physical tank, waves are generated using a flap wavemaker motion obtained by applying the wavemaker linear transfer function to each wave component (Dean and Dalrymple, 1990). As in the physical tank, both was generation and absorptions are imperfect and, in particular, there are some reflected waves, which are re-reflected at the wavemaker; additionally, the linear wavemaker transfer function for periodic waves only approximates the generation of nonlinear irregular waves. Accordingly, in Table 2, we find that both the targeted and measured H_s and L_p values show increasing differences, the larger wave nonlinearity.

	H_s (m)		L_p (m)		H_s/L_p (%)	
	target	actual	target	actual	target	actual
A	0.020	0.020	1.56	1.487	1.281	1.304
B	0.040	0.040	1.56	1.560	2.562	2.548
C	0.060	0.061	1.56	1.523	3.844	3.917
D	0.080	0.075	1.56	1.599	5.125	4.475
E	0.100	0.082	1.56	1.421	6.406	6.020

Table 2: Parameters of sea state spectra used to evaluate the WRP models in wave tank/NWT, targeted and actual values achieved (here) in NWT. In all cases, $T_p = 1$ s and $h_0 = 1.4$ m.

For all of the results presented here, the input parameters for the WRP algorithm are kept constant, in particular: $\Delta t_a = 12T_p$, $x_e = 2L_p$ (with $x_7 = 0$), $N = 100$ (wave components in the WRP models), $R = 9$ (overlapping realizations). For the latter, using a single NWT run for each wave case in Table 2, these realizations are obtained by selecting time series separated by $5T_p$. Note, time series of elevation misfit error $\mathscr{E}$ were smoothed using a moving average filter. As indicated, due to the limited space in this paper, we only report and compare the NWT results with the WRP predictions. Moreover, we only present detailed results for case **C**, which has a meaningful but still moderate nonlinearity, while for other cases, which have qualitatively similar time series, only the overall misfit metrics are presented in summary figures.

RESULTS

Figure 6 compares the time series of surface elevations reconstructed using each WRP model, for a single realization of case **C** in Table 2, to the NWT elevations, at the float location x_e. Similar time series would be acquired by the DT-MPC model, to be part of the control system actuation (see, Steele et al., 2023). Here, the reconstruction is

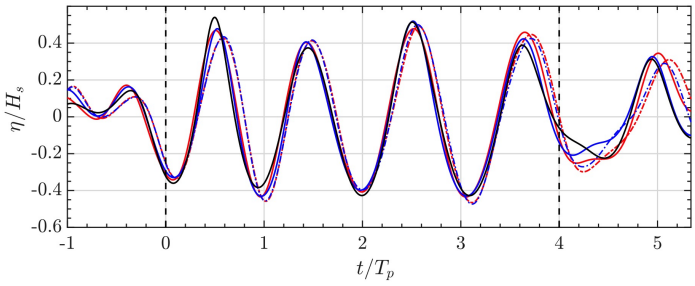

Fig. 6: Case **C** in Table 2 (acquisition time, $\Delta t_a = 12T_p$; float location, $x_e = 2L_p$). Comparison of (back-solid) NWT with wave WRP results at the float, using: (red-chained) LWT; (red-solid) LWT-CDR; (blue-chained) CWM; and (blue-solid) ICWM. The nonlinear phase shift for the LWT-CDR and ICWM models, better aligns waves with the NWT reference data. See also Fig. 9. Vertical dash lines mark the boundaries of the prediction zone $[t_{min} = 0, t_{max}]$ (Fig. 4).

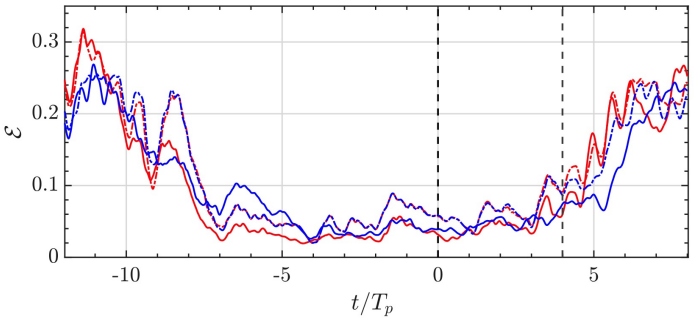

Fig. 7: Same case and line definitions as in Fig. 6. Time series of ensemble-averaged surface elevation misfit $\mathscr{E}$ at $x = x_e$. Dash lines mark theoretical boundaries of prediction zone $[t_{min} = 0, t_{max}]$ (Fig. 4).

based on a spatiotemporal data set acquired at gauges 1-7 (Table 1) for $t \in [-\Delta t_a, 0]$. As seen in Fig. 4, wave predictions based on a complete set of wave components can be issued at $x = x_e$ for $t \in [t_{min} = 0, t_{max}]$, with $t_{max} = (x_e - x_1)/c_{g1}$. Overall, the surface elevations predicted by the different WRP models all appear to be quite reasonable. However, models featuring nonlinear phase corrections appear more accurate (LWT-CDR and ICWM). This is further detailed next.

Additional realizations of wave predictions similar to Fig. 6 were generated for the same sea states, by re-initializing and applying the WRP models when shifting the acquisition time interval by $5T_p$ to the future, several times over the overall time series of NWT data. Thus, for nine such realizations ($R = 9$), Fig. 7 shows ensemble-averaged time series of surface elevation misfit $\mathscr{E}$ at $x = x_e$. As expected, a low misfit is achieved within the prediction zone, which slightly increases with time, i.e., with how far in the future the prediction is issued. For $x_e = 2L_p$, which corresponds to time $t = 2T_p$ for the dominant waves in the sea state, the misfit at this time is about 5% of H_s.

Figures 8 and 9 finally compare the elevation and phase misfits, time-averaged over the prediction zone $[0, t_{max}]$, for the different WRP models applied to the 5 sea state cases in Table 2, with have increasing nonlinearity. Overall, for the elevation misfit, the best results are obtained using ICWM with $\mathscr{E}^F \leq 2\%$ for all nonlinearity, while LWT-CDR performs almost as well, with less than 2.6%. Errors with the LWT and CWM models are larger in all cases, by at least 50%. For the phase misfit, Fig. 9 shows that tusing models with a nonlinear phase correction is more important, with $\mathscr{E}^P \leq 1\%$ for all nonlinearity, except for ICWM in case **E** where it is 1.8%. In contrast, the LWT and CWM models show an increasing phase misfit with nonlinearity, reaching 5% in case **E**.

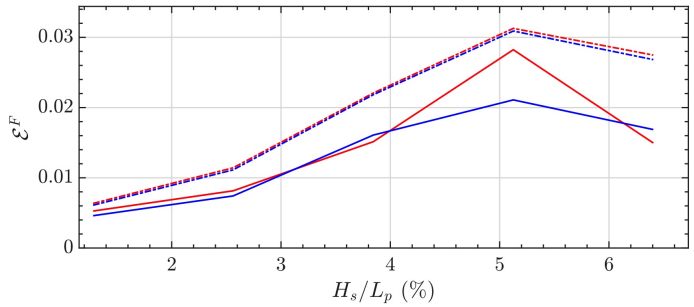

Fig. 8: Same case and line definitions as in Fig. 6. Average $\mathscr{E}^F$ of surface elevation misfit $\mathscr{E}$ at $x = x_e$, over prediction time interval $[0, t_{max}]$.

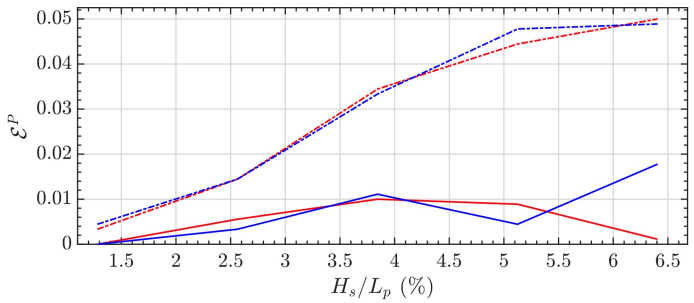

Fig. 9: Same case and line definitions as in Fig. 6. Ensemble-averaged surface elevation phase misfit $\mathscr{E}^P$ at $x = x_e$.

DISCUSSION AND CONCLUSIONS

The present work was performed in the context of a research project aimed at improving the active control of FOWT motions in irregular waves, by remotely sensing, forecasting, and assimilating future wave loading into the DT model and MPC algorithm used to actuate the control system. On this basis, a series of WRP models were developed, applied, and validated, based on spatiotemporal LiDAR-like wave datasets (i.e., that could have been remotely sensed by a LC), to reconstruct and propagate nonlinear irregular waves to a different location (i.e., that of the float) and future time, compared to where the data was acquired. For this approach to work, the WRP models need to be both accurate, particularly in their prediction of wave phases at the float, and sufficiently efficient to allow for a real time framework that provides sufficient lead time to the DT-MPC system to compute and issue the actuation law to the control system, before the considered waves have reached the FOWT. Due to a lack of space, only results of numerical validations of the WRP models, in comparison with results of a NWT, were presented. Aspects of DT-MPC development and application are detailed in our companion paper Steele et al. (2023), as well as experimental data and verifications.

Consistent with earlier work performed by some of the authors (e.g., Desmars et al., 2020), our results show that the nonlinear phase corrections included in the LWT-CDR and ICWM models appears to provide a significant sufficient reduction of phase misfits observed without those. Among these two models, while its predictions of surface elevations may be less accurate, the LWT-CDR model appears to predict wave phases adequately and hence would be preferred for its higher efficiency, although it still requires to perform iterations.

A key aspect of developing a real time WRP algorithm is flexibility in different operating conditions, which is a feature that was built into our operating procedure. Thus, the amount of data (i.e., number of spatial locations and temporal duration of the wave data set) used to issue a prediction can be adjusted depending on the spectral content of the sea state and configuration of the wave measurements. In practice, the character-

istics of the computer hardware, which the WRP algorithm runs on, will also provide information on how best select WRP parameters to optimize run time while still achieving an accurate prediction.

Some aspects of this work, not detailed here, that are still in development are how to best cope with uncertainty, aleatory in measurements and epistemic in model physics, to issue a safe control command to the FOWT control system. In this respect, errors on the phasing of wave loads are the main concern since a phase mismatch could cause larger motion and forces on the FOWT than without control, which negatively affects structural life and defeats the purpose of using such as control system. Hence, the selected WRP/model algorithm also needs to provide an estimate of the confidence of its prediction along with the prediction itself. Other authors (e.g., Zhang et al., 2022) implemented a Bayesian machine learning approach, which also determines a confidence interval for the wave prediction, but this approach being data-driven and non-physical also has its own limitations. Furthermore, the issue of noisy data in an experimental/field setting is an additional major factor. Here, although we acquired experimental data, we provided results and error estimates based on ideal data obtained with a highly accurate NWT. Desmars et al. (2020), who proceeded similarly but using a HOS model, also validated their WRP predictions using noisier wave tank data and found this in general increased the prediction errors, although these still stayed quite reasonable. This aspect will be crucial for the future field deployment of this system using a LC for acquiring wave data.

ACKNOWLEDGMENTS

The authors gratefully acknowledge support for this work from grant # DE-SC0022103 of the United States Department of Energy (DOE).

REFERENCES

Babarit, A. and Clément, A. H. (2006). Optimal latching control of a wave energy device in regular and irregular waves. *Applied Ocean Research*, 28(2):77–91.

Blondel-Couprie, E., Bonnefoy, F., and Ferrant, P. (2013). Experimental validation of non-linear deterministic prediction schemes for long-crested waves. *Oc. Engng.*, 58:284–292.

Casanovas, C. (2014). *Advanced Controls for Floating Wind Turbines*. PhD thesis, Massachusetts Institute of Technology, Cambridge, MA.

Dannenberg, J., Hessner, K., Naaijen, P., van den Boom, H., and Reichert, K. (2010). The on board wave and motion estimator owme. *Proc. Intl. Offsh. and Polar Engng. Conf.*, 3:424–431.

Dean, R. and Dalrymple, R. (1990). Water waves for engineers and scientists. advanced series on ocean engineering–.

Desmars, N., Bonnefoy, F., Grilli, S., Ducrozet, G., Perignon, Y., Guérin, C.-A., and Ferrant, P. (2020). Experimental and numerical assessment of deterministic nonlinear ocean waves prediction algorithms using non-uniformly sampled wave gauges. *Oc. Engng.*, 212:107659.

Dommermuth, D. G. and Yue, D. K. P. (1987). A high-order spectral method for the study of nonlinear gravity waves. *J. Fluid Mech.*, 184:267–288.

Ducrozet, G., Bonnefoy, F., Le Touzé, D., and Ferrant, P. (2016). HOS-ocean: Open-source solver for nonlinear waves in open ocean based on High-Order Spectral method. *Computer Phys. Com.*, 203:245–254.

Faedo, N., Olaya, S., and Ringwood, J. V. (2017). Optimal control, MPC and MPC-like algorithms for wave energy systems: An overview. *Journal of Systems and Control*, 1:37–56.

Fusco, F. and Ringwood, J. V. (2010). Short-term wave forecasting for real-time control of wave energy converters. *IEEE Trans. Sustain. Energy*, 1(2):99–106.

Grilli, S., Guérin, C.-A., and Goldstein, B. (2011a). Ocean Wave Reconstruction Algorithms Based on Spatio-emporal Data Acquired by a Flash LiDAR Camera. *Proc. 21st Intl. Offsh. and Polar Engng. Conf.*, pages 275–282.

Grilli, S. T., Grilli, A., Bastien, S. P., Sepe, R. B., and L, S. M. (2011b). Small buoys for energy harvesting: Experimental and numerical modeling studies. *Proc. 21st Intl. Offsh. and Polar Engng. Conf.*, pages 598–605.

Grilli, S. T. and Horrillo, J. (1997). Numerical generation and absorption of fully nonlinear periodic waves. *J. of Engng. Mech.*, 123(10):1060–1069.

Grilli, S. T., Horrillo, J., and Guignard, S. (2020). Fully nonlinear potential flow simulations of wave shoaling over slopes: Spilling breaker model and integral wave properties. *Water Waves*, 2(2):263–297.

Grilli, S. T. and Subramanya, R. (1996). Numerical modeling of wave breaking induced by fixed or moving boundaries. *Comput. Mech.*, page 374–391.

Guérin, C.-A., Desmars, N., Grilli, S. T., Ducrozet, G., Perignon, Y., and Ferrant, P. (2019). An improved lagrangian model for the time evolution of nonlinear surface waves. *J. Fluid Mech.*, 876:527–552.

Hals, J., Falnes, J., and Moan, T. (2011). Constrained optimal control of a heaving buoy wave-energy converter. *J. Offsh. Mech. Arctic Engine.*, 133(1):011401.

Kim, I.-C., Ducrozet, G., Bonnefoy, F., Leroy, V., and Perignon, Y. (2023). Real-time phase-resolved ocean wave prediction in directional wave fields: Enhanced algorithm and experimental validation. *Ocean Engineering*, 276:114212.

Ma, Y., Sclavounos, P. D., Cross-Whiter, J., and Arora, D. (2018). Wave forecast and its application to the optimal control of offshore floating wind turbine for load mitigation. *Renewable Energy*, 128:163–176.

Naaijen, P., Blondel-Couprie, E., and Delft University of Technology, t. N. (2012). Wave induced motion prediction as operational decision support for offshore operations. In *Marine Heavy Transport and Lift 2012*, page 11–18. RINA.

Naaijen, P., Trulsen, K., and Blondel-Couprie, E. (2014). Limits to the extent of the spatio-temporal domain for deterministic wave prediction. *International Shipbuilding Progress*, 61:22.

Nouguier, F., Chapron, B., and Guérin, C.-A. (2015). Second-order lagrangian description of tri-dimensional gravity wave interactions. *J. Fluid Mech.*, 772:165–196.

Nouguier, F., Grilli, S., and Guérin, C.-A. (2014). Nonlinear ocean wave reconstruction algorithms based on simulated spatiotemporal data acquired by a flash lidar camera. *IEEE Trans. on Geosci. and Remote Sensing*, 52:1761–1771.

Nouguier, F., Guérin, C.-A., and Chapron, B. (2009). "choppy wave" model for nonlinear gravity waves. *J. Geophys. Res.*, 114(C9):C09012.

Steele, S. C., Albertson, S., Fontaine, J., Dahl, J. M., Grilli, S. T., Hashemi, R. M., Alkarem, Y. R., Kimball, R. W., and Hejrati, B. (2023). Active control of the wave-induced motions of a float: Real-time simulations with a digital twin and experimental validation. In *Proc. 33rd Intl. Offsh. and Polar Engng. Conf.* ISOPE.

Wu, F., Zhang, X., and Sterling, M. (2009). Optimal control for aws-based wave energy conversion system. *IEEE Transactions on Power Systems*, 24(4):1747–1755.

Wu, G. (2004). *Direct Simulation and Deterministic Prediction of Large-scale Nonlinear Ocean Wave-field*. Phd, MIT.

Zhang, J., Zhao, X., Jin, S., and Greaves, D. (2022). Phase-resolved real-time ocean wave prediction with quantified uncertainty based on variational bayesian machine learning. *Applied Energy*, 324:119711.

Zou, S., Abdelkhalik, O., Robinett, R., Bacelli, G., and Wilson, D. (2017). Optimal control of wave energy converters. *Renewable Energy*, 103:217–225.